

Supplemental material

Operating conditions and thermodynamic bounds of dual radiative heat engines

Julien Legendre and Pierre-Olivier Chapuis
*Univ Lyon, CNRS, INSA-Lyon, Université Claude Bernard Lyon 1,
 CETHIL UMR5008, F-69621, Villeurbanne, France*
 (Dated: February 9, 2024)

I. ELECTRICAL CHARACTERISTIC OF OPTOELECTRONIC COMPONENTS

We provide in Figure S1 the current-voltage characteristic of the various optoelectronic components considered for dual radiative engines [1]. Two of them produce electrical power (TR and PV cells) while the two others consume power (LEDs and NEL diodes).

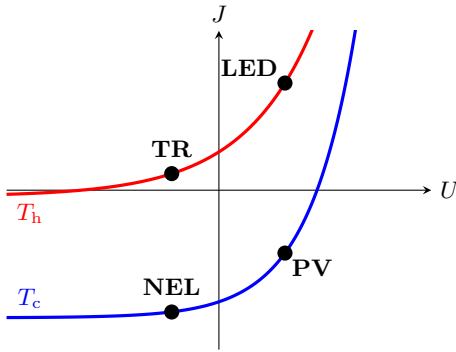


FIG. S1: Schematic of current-voltage characteristics of optoelectronic devices. $U \cdot J > 0$ means that electrical power is consumed.

II. PERFORMANCE OF DUAL ENGINES FOR LOW BANDGAPS

We provide in Fig. S2 the variation of electrical power output and cooling power as a function of both chemical potentials, this time for $E_g = k_B T_h$. In comparison to the results obtained for larger bandgaps, the gap between the heat engine and heat pump operating regions is larger. The change is particularly visible in the TPX quadrant, since then $E_g - \mu_i$ becomes lower than $k_B T_i$. In this quadrant, the device is almost always capable of operating as a heat engine as long as $\mu_c \geq \mu_h$. Consequently, TPX devices are not able to operate as heat pumps for such low bandgaps.

III. IMPACT OF NON-RADIATIVE LOSSES ON $\eta - P$ CHARACTERISTICS

The results presented in the main article are obtained at the radiative limit, and therefore provide an upper

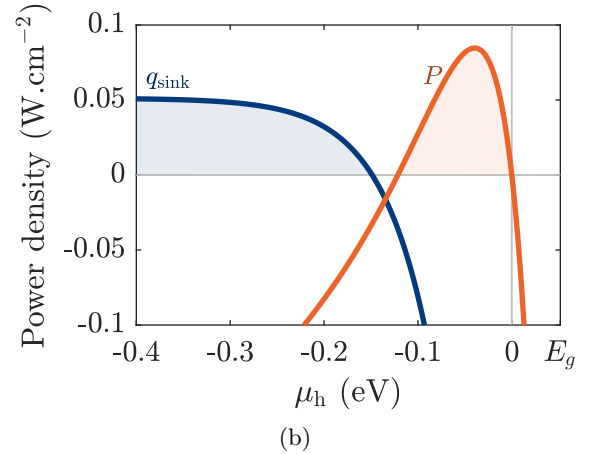
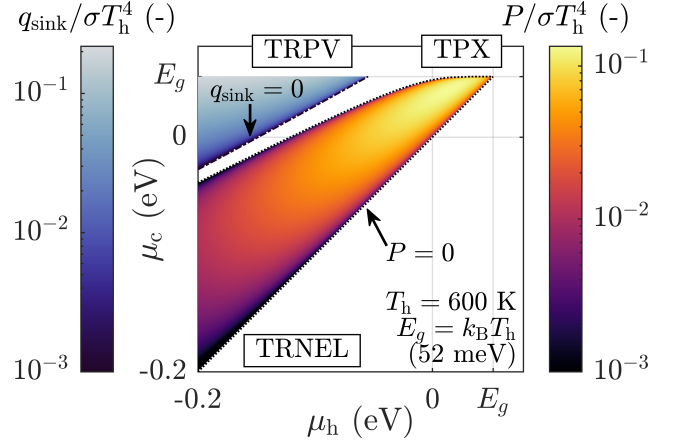


FIG. S2: (a) Performance of dual radiative systems operating as heat engines or heat pumps, at the radiative limit and for $E_g = k_B T_h = 52$ meV. (b) Zoom on the $\mu_c = 0$ scenario.

bound for dual radiative engines' performance. Obviously, if non-radiative losses are included, performance will be worsened: we aim at giving here some first insights about the impact of such losses. To do so, we manually set the quantum efficiency (QE), defined as the fraction of recombinations being radiative, to 0.9 for both components of the dual engine. This means that 10% of the total recombination rate can be attributed to non-radiative losses. Since the non-radiative generation rate must balance the non-radiative generation rate at equilibrium, we get a new expression of the power generated

by an optoelectronic component [2]:

$$P_i = \mu_i \left(\dot{N}_j - \dot{N}_i - \frac{1 - \text{QE}}{\text{QE}} \left(\dot{N}_i - \dot{N}_i(\mu_i = 0) \right) \right). \quad (1)$$

For a 600 K heat source temperature, the use of this expression leads to the $\eta - P$ plots illustrated in Fig. S3. Several major differences appear in comparison to the results obtained at the radiative limit. First, TRNEL devices have significantly lost interest, since they are no longer able to reach Carnot efficiency. Worse, their envelope is now within that of TRPV devices for both bandgaps considered. Therefore, TRNEL systems have interest only when operating close enough to the radiative limit. Second, the maximum efficiency is now highly dependent on the bandgap: being only 40% of Carnot efficiency for $E_g = k_B T_h$, it goes up to 80% of η_C for $E_g = 10k_B T_h$. Last, the power output variation with the bandgap is way weaker; in fact, as long as $\text{QE} < 1$, there is an optimal bandgap that allows maximising the power output [3] (page 61).

Additionally, including non-radiative losses causes a mismatch between the currents J_h and J_c of the two optoelectronic components. Since voltages are mismatched too, the two components cannot be directly bound electrically if both have the same area, and additional electronics is necessary to make the engine work. Otherwise, it is possible to design engines with components with mismatched areas [4] or bandgaps [5] to make them self-sustaining.

IV. IMPACT OF HEAT SOURCE TEMPERATURE ON $\eta - P$ CHARACTERISTICS

In Fig. S4 and S5 are provided $\eta - P$ plots obtained at the radiative limit, but respectively for a 400 K and 1200 K heat source temperature. The conclusion drawn for $T_h = 600$ K remains valid in these scenarios. We can still notice two slight differences. First, the normalised power output achieved becomes larger as T_h increases. Considering $E_g = 10k_B T_h$ for instance, $P_{\text{max}}/\sigma T_h^4$ equals approximately 0.6 for $T_h = 400$ K, but goes up to 2.4 for $T_h = 600$ K and exceeds 5 for $T_h = 1200$ K. Second, the interest of TRPV devices rises with temperature, more and more of the total envelope corresponding to that of the TRPV device if the bandgap stays moderate. For $T_h = 1200$ K and $E_g = k_B T_h \approx 0.1$ eV, TRPV gives access to interesting trade-offs between power and efficiency. However, note that such high temperatures can hardly be withstood by optoelectronic components, and therefore limits TRPV interest.

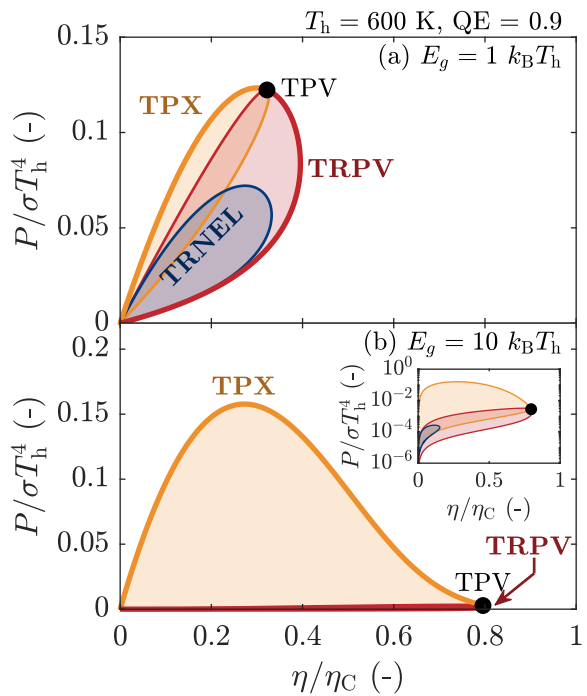


FIG. S3: $\eta - P$ plots obtained for dual radiative engines, for $T_h = 600$ K and for various bandgaps. A quantum efficiency of 0.9 is considered.

V. VARIATION OF MAXIMUM POWER AND RELATED EFFICIENCY WITH BANDGAP

We provide in Fig. S6 the variations of the maximum power and related efficiency as a function of the bandgap, respectively for the complete dual engine (thick black line) and for each individual engine. For a heat source temperature of 600 K, the dual engine MPP moves from the TRPV quadrant for low bandgaps to the TPX quadrant for higher bandgaps. In this case, the transition between the two quadrants occurs around $E_g/k_B T_h = 0.7$. Dual engines become especially attractive when $E_g > k_B T_h \approx 0.05$ eV, their power output increasing with E_g and being already 50% larger than that of single engines for $E_g = 1.9k_B T_h$. In practice, this condition is satisfied by any realistic bandgap at the temperature considered.

Note how, when TPX or TRPV engines do not maximise the power output, they operate as TPV devices. This is what causes the sudden change in slope observable in panel (b): around $E_g/k_B T_h = 0.7$, there is for both devices an abrupt change in the direction of displacement of the MPP in (μ_h, μ_c) coordinates, from that of the complete dual engine to that of a TPV device (or vice-versa).

One can also observe that optimising TRNEL devices for electrical power production simply means operating as a TR device. Moreover, in the limit of zero bandgap, TR operation becomes optimal: this is because the TRNEL quadrant is the only one available since $\mu < E_g \rightarrow 0$.

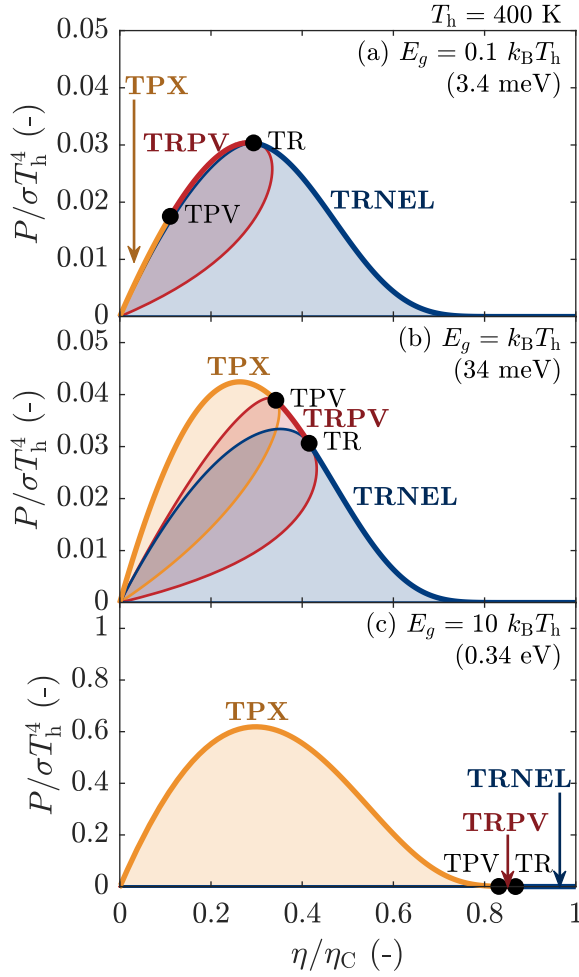


FIG. S4: $\eta - P$ plots obtained for dual radiative engines at the radiative limit, for $T_h = 400$ K and for various bandgaps.

VI. DETERMINATION OF THE CHEMICAL POTENTIALS AT MAXIMUM POWER

The goal is to determine the couple (X_h, X_c) which allows maximising P :

$$P = \frac{E_g^2 k_B^2 T_h^2}{4\pi^2 c^2 \hbar^3} \left(\ln(X_h) - \frac{T_c}{T_h} \ln(X_c) \right) \times \left(\ln(1 - X_h) - \frac{T_c}{T_h} \ln(1 - X_c) \right). \quad (2)$$

The first thing to verify is whether the maximum power is reached inside the domain (i.e. for $0 < X_i < 1$) or at the boundary. For instance, if X_h goes to 0, it gives

$$P \sim -\frac{E_g^2 k_B^2 T_h^2}{4\pi^2 c^2 \hbar^3} \ln(X_h) \ln(1 - X_c) \frac{T_c}{T_h} \rightarrow -\infty, \quad (3)$$

and the maximum power is therefore not reached at this boundary (the power being negative). A similar treatment can be done at the three other boundaries to ensure

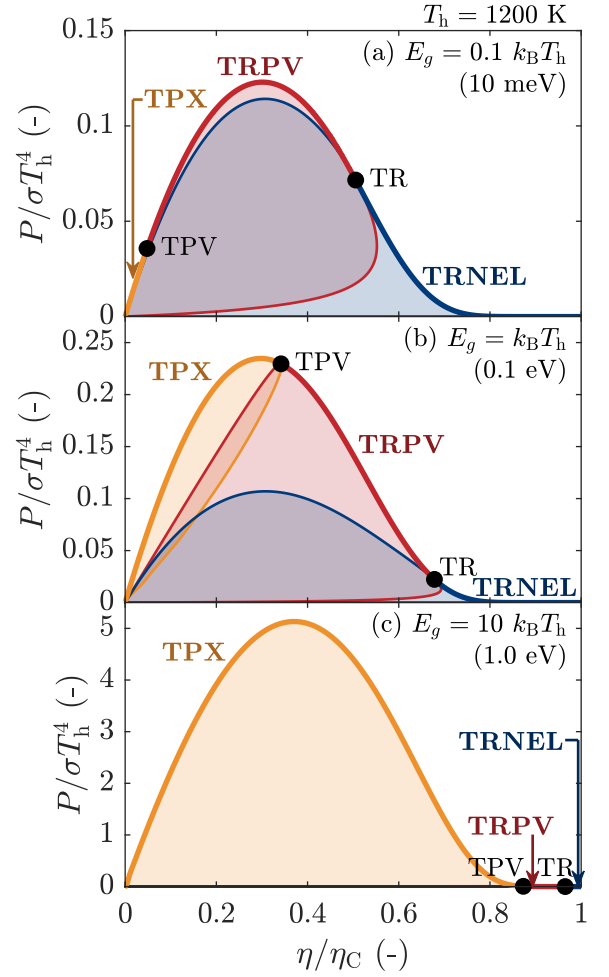


FIG. S5: $\eta - P$ plots obtained for dual radiative engines at the radiative limit, for $T_h = 1200$ K and for various bandgaps.

that the maximum power point is indeed located inside the domain. We should then find the couple (X_h, X_c) which makes both partial derivatives equal to zero. If the couple found is unique, it is the maximum power point since P goes to $-\infty$ at the boundaries (which means that a maximum power point must exist).

Setting both partial derivatives of P with respect to X_i to zero, we get

$$\frac{\ln(1 - X_h) - \ln(1 - X_c) \frac{T_c}{T_h}}{\ln(X_h) - \ln(X_c) \frac{T_c}{T_h}} = \frac{X_h}{1 - X_h}, \quad (4a)$$

$$= \frac{X_c}{1 - X_c}. \quad (4b)$$

Note that this holds only if $\ln(X_h) - \ln(X_c) \frac{T_c}{T_h}$ is non-zero at the maximum power point. If the former term was equal to zero, then $\ln(1 - X_h) - \ln(1 - X_c) \frac{T_c}{T_h}$ should also be zero to satisfy that partial derivatives are equal to zero, which would lead to $1 - X_c^{T_c/T_h} = (1 - X_c)^{T_c/T_h}$. This equation being satisfied only for X_c equal to 0 or 1

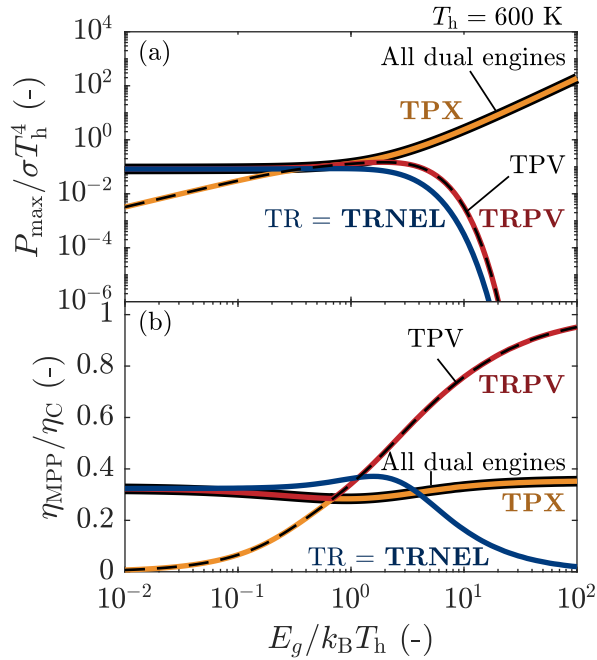


FIG. S6: Variation of (a) the maximum power, (b) the efficiency at maximum power, for the different radiative engines considering $T_h = 600$ K.

(which are not inside the domain), $\ln(X_h) - \ln(X_c) \frac{T_c}{T_h}$ is therefore non-zero at the maximum power point.

Combining the two expressions given in Eq. (4), we easily get that $X_h = X_c$. Writing this common value X , we obtain

$$P = \frac{1}{\hbar} \left(\frac{E_g k_B (T_h - T_c)}{2\pi c \hbar} \right)^2 \ln(X) \ln(1 - X). \quad (5)$$

Notice how P is symmetric around the axis $X = 1/2$ (since $P(X) = P(1 - X)$): at $(X_h = 1/2, X_c = 1/2)$, both partial derivatives therefore equal zero. In fact, this couple is the only possible solution, and corresponds thus to the maximum power point.

VII. IMPACT OF THE CHEMICAL POTENTIAL OF QUASI-MONOCROMATIC RADIATION

In the article, to derive an expression of the efficiency at maximum power in the case of quasi-monochromatic radiation exchanged, we state that $E_g - \mu_i \ll k_B T_i$. To verify this, we show in Fig. S7 the variation of power output with μ_h for $E_g = 1$ eV, considering only the TPX quadrant. The power output associated to each μ_h corresponds to the maximum achievable with the whole range of μ_c available. We observe that $E_g - \mu_{h,MPP} \ll k_B T_c$: since $T_h > T_c$, therefore $E_g - \mu_{h,MPP} \ll k_B T_h$. Moreover, $\mu_c \geq \mu_h$, and thus $E_g - \mu_{c,MPP} \ll k_B T_c$.

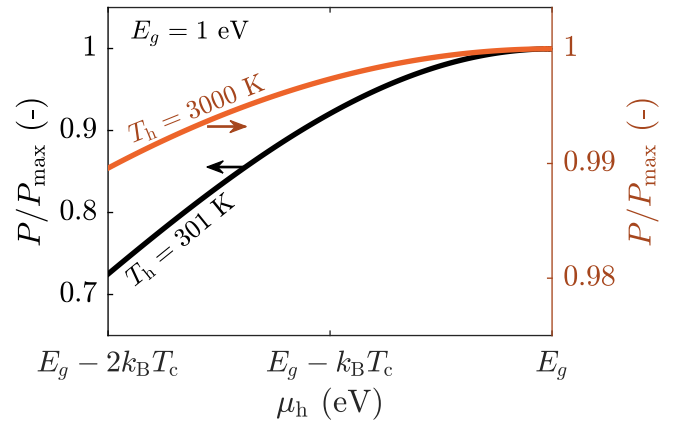


FIG. S7: Variation of the power output with the LED chemical potential considering quasi-monochromatic radiation exchanged, for $E_g = 1$ eV and for two heat source temperatures. In this case, only the TPX quadrant is considered.

VIII. MODIFICATION OF THE ACHIEVABLE OPERATING CONDITIONS UNDER SPECTRAL FILTERING

To study the impact of spectral filtering (i.e. of reducing the radiation bandwidth δE), we show in Fig. S8 how the $\eta - P$ envelope of dual engines vary with δE . In addition, the complete set of operating conditions achievable by varying δE is represented by the grey area. Three different scenarios are considered to highlight the variability of the influence of spectral filtering on the achievable operating conditions.

The envelopes obtained at the radiative limit for a bandgap of $k_B T_h$ are shown in panel (a), the results being mostly similar to those obtained at $E_g = 10 k_B T_h$. In this scenario, filtering gives access to new operating conditions in the high-efficiency region. For $P/\sigma T_h^4 < 0.03$, this can allow increasing the efficiency by up to 10 percent points. The effect is even stronger when decreasing the quantum efficiency (QE) to 0.9 (see Section III for more details on QE), as depicted in panel (b): an efficiency increase of the order of 25 percent points can be reached for $P/\sigma T_h^4 = 0.03$, and goes up to 45 percent points for $P/\sigma T_h^4 = 0.01$. In this case, the MPP obtained with filtered radiation can even move beyond the envelope obtained in the broadband scenario. In other words, spectral filtering can limit the power loss undergone in high-efficiency operation.

There are however cases where filtering has no significant benefit. We provide one such example in panel (c), obtained for $QE = 0.9$ and $E_g = 10 k_B T_h$. Under such conditions, reducing the bandwidth mostly make the envelope shrink, the only benefit being a small increase of the efficiency achieved for powers close to zero. In such scenarios, it is thus better to prevent filtering radiation.

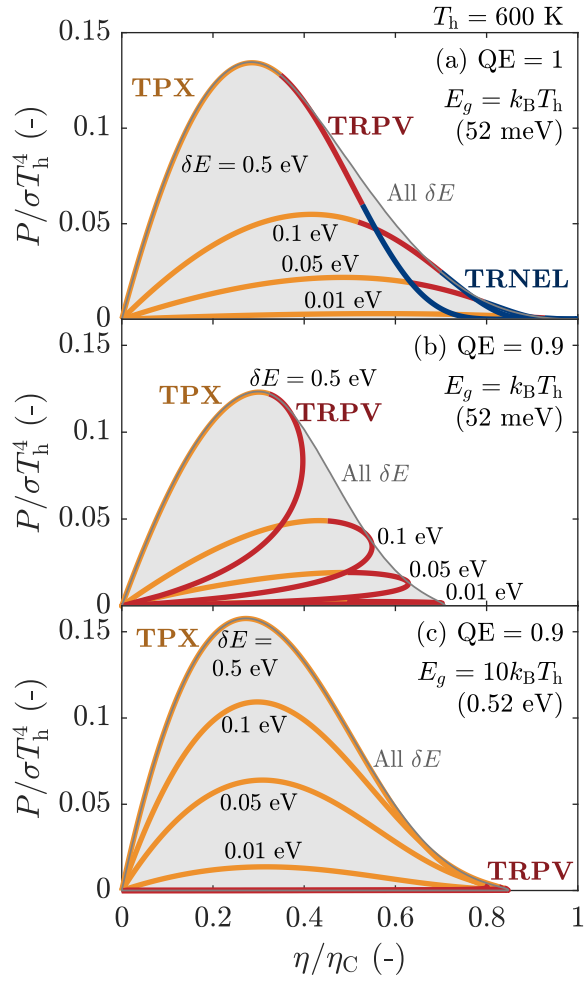


FIG. S8: Dual radiative engine $\eta - P$ envelopes obtained for varying spectral bandwidth δE .

- [1] E. J. Tervo, E. Bagherisereshki, and Z. M. Zhang, Near-field radiative thermoelectric energy converters: a review, *Frontiers in Energy* **12**, 5 (2018).
- [2] J. Legendre and P.-O. Chapuis, GaAs-based near-field thermophotonic devices: Approaching the idealized case with one-dimensional PN junctions, *Solar Energy Materials and Solar Cells* **238**, 111594 (2022).
- [3] J. Legendre, *Theoretical and numerical analysis of near-field thermophotonic energy harvesters*, Ph.D. thesis, INSA Lyon, available at <https://theses.fr/2023ISAL0094> (2023).
- [4] B. Zhao, S. Buddhiraju, P. Santhanam, K. Chen, and S. Fan, Self-sustaining thermophotonic circuits, *Proceedings of the National Academy of Sciences* **116**, 11596 (2019).
- [5] Z. Yang, J. Song, and B. J. Lee, Thermophotonic cells in self-sustaining parallel circuits, *Journal of Quantitative Spectroscopy and Radiative Transfer* **312**, 108792 (2024).